Novel insights into heterogeneous nucleation interface properties between La_2O_3 and γ-TiAl: First-principles calculations

Qizhen He [a], Jibo Wang [b], Wenwei Song [a], Yuenian He [a], Xuejun Ren [c], Jing Guo [d], Qin gxiang Yang [a]

a: State Key Laboratory of Metastable Materials Science & Technology, Hebei Key Lab for Optimizing Metal Product Technology and Performance, Yanshan University, Qinhuangdao 066004, PR China

b: Fujian Provincial Key Laboratory of Welding Quality Intelligent Evaluation, Longyan University, Longyan 364012, PR China

c: School of Engineering, Liverpool John Moores University, Liverpool L3 3AF, UK

d: Henry Royce Institute for Advanced Materials, The University of Manchester, Manchester M19 3PL, UK

Abstract

The refinement effect of the rare earth oxide La_2O_3 on γ-TiAl by first-principles method was investigated in this study. The mismatch between different low-index interfaces of La_2O_3 and γ-TiAl was calculated, and the interface with the smallest mismatch was selected to construct the La_2O_3/γ-TiAl interface. The stability and electronic structure of the interface were assessed, and the efficacy of La_2O_3 as a heterogeneous nucleation core for γ-TiAl was analyzed. The results reveal that the La_2O_3 (100)/γ-TiAl(100) interface displays the smallest mismatch, which is 4.36 %. Four La_2O_3 (100)/γ-TiAl(100) interface models were constructed based on various surface terminations and stacking sequences. Among these models, the O-Al model exhibits the highest interfacial binding energy of 5.062 J/m^2, while the O-Ti model demonstrates the lowest interfacial energy of −3.300 J/m^2. The primary bond type in the interface models is ionic bonding. Therefore, from the geometric and energetic aspects of the interface structure, it can be inferred that La_2O_3 can act as a heterogeneous nucleation core for refining the γ-TiAl phase, with a preference for forming O-Ti type heterogeneous nucleation interfaces.

1. Introduction

TiAl alloys, as a new generation of the high-temperature structural materials, demonstrate exceptional high-temperature mechanical properties and low density, which are highly suitable for applications in aerospace and various other industries [1], [2], [3]. However, its room-temperature brittleness and inadequate strength at middle and high temperatures limit its wide application in the aerospace industry [4], [5].

The microstructure of TiAl alloy mainly consists of γ-TiAl and α_2-Ti_3Al phases [6], [7]. The γ-TiAl phase is classified as an intermetallic compound with an ordered face-centered cubic crystal structure, which offers the alloy low density, high strength, and exceptional high-temperature characteristics. However, the α_2-Ti_3Al phase, known for its higher density, exhibits inadequate oxidation resistance. As a result, the mechanical properties of the TiAl alloy are primarily determined by the γ-TiAl phase [8].

In recent years, the significant research efforts have been dedicated to enhance the mechanical properties of TiAl alloys by alloying method[9]. Kim and Yasuda [10], [11] observed that the Nb elements activates all deformation mechanisms of the γ-TiAl phase during the deformation process, so that the room temperature plasticity of TiAl alloys can be improved. Furthermore, the Nb elements raises the yield strength of the γ-TiAl intermetallic compound to 371 MPa. Shu et al. [12] investigated the effect of dopant elements Fe, Co, and Ni on the ductility of the γ-TiAl intermetallic compound. It was found that doping with Fe and Co can improve both the ductility and strength of the γ-TiAl intermetallic compound. While, Ni doping reduces its ductility. These research results suggest that alloying elements, particularly Nb, have a beneficial effect on the mechanical properties of the γ-TiAl intermetallic compound. However, the challenges such as room temperature brittleness and inadequate strength at middle and high temperatures still persist [13], [14].

By refining the microstructure of alloys, not only can the yield strength and tensile strength of the alloys be enhanced, but also their ductility can be improved simultaneously [15]. Currently, the application of the microstructure refinement techniques to enhance the overall mechanical properties of the alloys has attracted significant attention [16].

The rare earth oxides added into alloys can play a significant role in refining, purifying, and modifying the alloys, which results in notable improvements in mechanical properties of the alloys [17], [18], [19]. Wang et al. [20], [21] examined the effect of CeO_2 on the wear and corrosion resistance of Ni-based alloy. They found that it can refine the microstructure, increase the hardness, enhance the wear resistance, and improve the corrosion resistance of the alloy. Zhao et al. [22] studied the influence of La_2O_3 on iron-based alloys, it was observed that the La_2O_3 can refine the microstructure of the iron-

based laser cladding coating and significantly enhance the corrosion resistance of the coating. Therefore, it is suggested that in TiAl alloys, the γ-TiAl phase maybe refined by the rare earth oxides, which can enhance the mechanical properties of TiAl alloys. To research the refining effect of rare earth oxides on γ-TiAl phase, it is necessary to establish the interfacial relationship between rare earth oxides and the γ-TiAl phase. However, it is impossible to clarify the interface relationship and refinement mechanism between rare earth oxides and the γ-TiAl phase by experimental.

Currently, the first-principles method based on density functional theory has become a crucial one for investigating the surface and interface properties of materials [23], [24]. Pei et al.[25] conducted a study using first-principles methods to explore the tensile properties and fracture mechanisms of the Al(111)/Al_3Ti(112) interface. The results revealed that with increase of the tensile strain, significant areas of the electron holes emerge at both the interface and sub-interface, which lead to a substantial weakening of the atomic interactions. When the strain is exceeded 25 %, the fractures appear in the Al-Ti and Al-Al bonds at the interface, which results in the failure of the tensile model. Dai [26] investigated the stability and effect of alloying elements on the TiAl/TiO_2 interface via first-principles calculations. The results demonstrated that elements Y, Nb, and Pd can enhance the adhesion energy between TiO_2 and TiAl, which prevents the detachment of the oxide layer and enhances the cyclic oxidation resistance of TiAl. Therefore, it is feasible to investigate the interfacial relationship between rare earth oxides and γ-TiAl by first-principles method.

In this study, the typical rare earth oxide La_2O_3 was selected, and the mismatch between La_2O_3 and γ-TiAl on various low-index surfaces was calculated by first-principles method. An interface model of La_2O_3/γ-TiAl was established to assess the stability, interfacial binding energy, interfacial energy, and electronic structure of the interface. The efficacy of La_2O_3 as a heterogeneous nucleation core for γ-TiAl was investigated.

2. Computational method

All calculations in this study were conducted using the Vienna Ab-initio Simulation Package (VASP) within the framework of Density Functional Theory (DFT) [27], [28]. The Perdew-Burke-Ernzerhof generalized gradient approximation (GGA-PBE) [29], [30] exchange-correlation functionals were adopted to describe exchange-correlation energy for the calculation, and the interaction between ions and valence electrons was treated separately. For the structural optimization, the positions of all atoms were allowed to relax freely until the total energy and force converge to 10^{-5} eV/atom and 0.001 eV/ Å, while the shape and volume of the unit cell were preserved. Convergence tests were performed on Encut and Kpoints to ensure calculation accuracy. And the sampling Kpoints mesh grid in the Irreducible Brillouin Zone (IBZ) was obtained by Monkhorst-Pack method [31]. The convergence criteria were set with an energy threshold of 1.0×10^{-5} eV/atom and Hellmann-Feynman force is allowed as low as 0.02 eV/atom. Encut and Kpoints settings were examined for La_2O_3 and γ-TiAl, with detailed calculation procedures illustrated in Fig. 1. The specific parameters chosen for Encut and Kpoints in the computations of the bulk phase model, surface model, and interface model are listed in Table 1.

3. Results and analysis

3.1. Determination of interface relationship between La_2O_3 and γ-TiAl

3.1.1. Bulk phase structure of La_2O_3 and γ-TiAl

Before computing the surface properties of La_2O_3 and γ-TiAl, it is crucial to fully relax their bulk phase structures to achieve optimal stability. The crystal structures of La_2O_3 and γ-TiAl are illustrated in Fig. 2**.** Fig. 2**(a)** displays that the crystal structure of La_2O_3. La_2O_3 is identified as belonging to the P-3m1(164) space group, with lattice constants a = b = 3.938 Å and c = 6.173 Å, v =82.899 $Å^3$ following relaxation. These values closely match with those reported in previous experimental [32] and computational [33] references. Fig. 2**(b)** displays the crystal structure of γ-TiAl, which belongs to the P4/mmm(123) space group. After relaxation, γ-TiAl exhibits lattice parameters of a = b = 4.019 Å and c = 4.065 Å, v =65.659 $Å^3$. These values closely match with those reported in earlier experimental [34] and computational [35] references. These results affirm the accuracy of the La_2O_3 and γ-TiAl unit cells utilized in this study, which have been widely accepted in the literature and produce reliable results, therefore it meets the computational requirements of this study.

The band structure and density of states diagram of La_2O_3 are shown in Fig. 3**.** Fig. 3**(a)** presents the band structure of La_2O_3 with the Fermi level marked by the dashed line. It is evident that the band structure of La_2O_3 does not intersect the Fermi level, and there exists a distinct band gap width between the valence and conduction bands. Since the valence band maximum and conduction band minimum of La_2O_3 are not directly aligned, it indicates the semiconductor characteristics of La_2O_3 with an indirect band gap.

Fig. 3**(b)** presents the total density of states and partial density of states diagram for La_2O_3. It can be observed that there is no density of states peak at the Fermi level, which indicates its non-metallic nature. Within the range from −17 eV to −10 eV, the total density of states peaks primarily originate from various orbitals of La atoms, with contributions from the s orbital of O atoms and the p orbital of La atoms exhibiting orbital resonance and hybridization effects, it suggests the formation of chemical bonds with certain covalent characteristics. The density of states peaks from −4 eV to the Fermi level mainly derive from the p orbital of O atoms, which resonates with the d orbital of La atoms. The weak intensity of La atom peaks suggests the migration of outer electrons from La atoms towards more electronegative O atoms. The discrepancy between the density of states centers of La d orbitals and O p orbitals indicates strong ionic bonding. Therefore, the chemical bonding in the bulk structure of La_2O_3 comprises a hybrid mixture of covalent and ionic bonds.

The band structure and density of states diagram of γ-TiAl are shown in Fig. 4. Fig. 4**(a)** presents the band structure of γ-TiAl, with the Fermi level denoted by a dashed line. It is evident that the band structure of γ-TiAl intersects the Fermi level, which indicates the presence of the electrons capable of transitioning from the valence band to the conduction band, therefore, it demonstrates the metallic properties of γ-TiAl.

Fig. 4**(b)** presents the total density of states and partial density of states for each atom in γ-TiAl. It is observed that γ-TiAl shows sharp peaks in the density of states at the Fermi level, which implies the existence of the metallic bonds primarily originating from the d orbitals of Ti atoms. In the vicinity ranging from −4 eV to near the Fermi level, the resonance and orbital hybridization between the p orbitals of Al atoms and the d orbitals of Ti atoms suggest the formation of covalent bonds. Consequently, the chemical bonding in the bulk structure involves the establishment of metallic and covalent bonds.

The Voigt-Reuss-Hill (VRH)[36] approximation was employed to compute the bulk modulus (B), shear modulus (G), Young's modulus (E), and Poisson's ratio (v) of the γ-TiAl and La_2O_3 crystal structures. The calculation results of the stiffness matrix C_{ij} are as follows:

The computational formula of the elastic matrix for γ-TiAl is as follow:

$$C_{ij}(GPa)=\begin{vmatrix} 186 & 90 & 89 & & & \\ 90 & 186 & 89 & & & \\ 89 & 89 & 179 & & & \\ & & & 76 & & \\ & & & & 76 & \\ & & & & & 76 \end{vmatrix} \quad (1)$$

The computational formula of the elastic matrix for La_2O_3 is as follow:

$$C_{ij}(GPa)=\begin{vmatrix} 220 & 122 & 92 & & -33 & \\ 122 & 220 & 92 & & 33 & \\ 92 & 92 & 142 & & & \\ & -33 & 33 & 60 & & \\ & & & & 60 & -33 \\ & & & & -33 & 51 \end{vmatrix} \quad (2)$$

Based on the elastic matrices of γ-TiAl and La_2O_3, a three-dimensional (3D) plot illustrating the anisotropy of their elastic properties was created [37]. The 3D plot demonstrating the anisotropy of γ-TiAl is shown in Fig. 5, where higher isotropic elastic properties lead to smaller variations in the contour surface of the 3D plot. It can be observed from the figure that the 3D surface plots of γ-TiAl display relatively regular solid shapes. The specific calculation results for the elastic constants of γ-TiAl are detailed in Table 2.

The 3D plot depicting the anisotropy of La_2O_3 is shown in Fig. 6, which reveals an irregular three-dimensional surface with significant differences in behavior between the [001] direction and the [100] and [010] directions. This discrepancy arises because La_2O_3 belongs to the P-3M1(164) space group, whereas γ-TiAl belongs to the P4/mmm(123) space group. The specific calculated results of the elastic constants of La_2O_3 are listed in Table 3. Comparison between Table 2 and Table 3**,** it shows that the anisotropy values of γ-TiAl for the Bluk modulus, Young's modulus, Shear modulus, and Poisson's ratio are all smaller than those of La_2O_3, which indicates that γ-TiAl exhibits weak anisotropy while La_2O_3 demonstrates relatively strong anisotropy. Notably, the anisotropy of the Bluk modulus of γ-TiAl is the smallest, which is 1.09, whereas the anisotropy of the Young's modulus of La_2O_3 is the largest, which is 3.55.

3.1.2. Lattice mismatch between La_2O_3 and γ-TiAl

From Bramfitt's two-dimensional lattice mismatch theory [38], it is known that when the misfit between the substrate and nucleation phases is less than 6 %, the substrate acts as the most effective heterogeneous nucleation site, which promotes a coherent interface. When the mismatch is between 6 % and 12 %, the substrate's nucleation effectiveness is moderate, which lead to a semi-coherent interface. When the mismatch is larger than 12 %, it precludes the substrate from serving as a nucleation site, and results in a non-coherent interface. Consequently, the crystal face combinations with minimal mismatch were selected, as guided by Bramfitt's theory, which facilitates the attainment of a more stable interface. The calculational formula for Bramfitt's two-dimensional lattice mismatch is as follow:

$$\delta^{(hkl)_s}_{(hkl)_n} = \frac{1}{3}\sum_{i=1}^{3}\frac{\left|d^i_{[uvw]_s}\cos\theta - d^i_{[uvw]_n}\right|}{d^i_{[uvw]_n}} \times 100\% \quad (3)$$

where, hkls denotes a low-index crystal plane in the substrate phase; uvws represents a low-index crystal direction within the crystal plane of the substrate phase; hkln stands for a low-index crystal plane in the nucleation phase; uvwn corresponds to a low-index crystal direction within the crystal plane of the nucleation phase; duvws indicates the atomic distance along the uvws direction in the crystal plane; duvwn represents the atomic distance along the uvwn direction in the hkln crystal plane.

The two-dimensional lattice mismatch between different low-index crystal planes of La_2O_3 and γ-TiAl are listed in Table 4. When their crystal orientations are La_2O_3(100) and γ-TiAl(100) respectively, the mismatch at the La_2O_3/γ-TiAl interface measures a minimal 4.36 %. This value falls within the most effective range for heterogeneous nucleation, which indicates that La_2O_3 meets the crystallographic criteria to serve as the most effective substrate for heterogeneous nucleation of γ-TiAl. Therefore, La_2O_3(100) and γ-TiAl(100) is recommended for constructing the interface.

3.1.3. Surface energy of La_2O_3 and γ-TiAl

Before constructing the interface model, it is crucial to determine the layer thickness of the La_2O_3 and γ-TiAl surface models. Based on the mismatch calculation results, the surface models of La_2O_3(100) and γ-TiAl(110) with varying thicknesses were developed. Convergence tests were performed on their surface energies to ascertain the minimum layer thicknesses required to achieve bulk-like properties. The La_2O_3(100) surface can be categorized into O-Terminated and OLa-Terminated surfaces, while the γ-TiAl(110) surface can be categorized into Al-Terminated and Ti-Terminated surfaces. To mitigate interactions between surface layers under periodic boundary conditions, a 15 Å vacuum layer was added in the surface and subsequent interface models. The diagrams illustrating the surface models of La_2O_3 and γ-TiAl are shown in Fig. 7.

Surface energy σ is the energy required to create a surface by separating it from the bulk structure. The surface energy calculational formula for La_2O_3(100) is as follow:

$$\sigma_{La_2O_3(100)} = \frac{1}{2A}[E_{slab} - N_{La}\mu_{La} - N_O\mu_O] \quad (4)$$

where $\sigma_{La_2O_3(100)}$ represents the surface energy of the La_2O_3(100) surface model; A is the surface area of the crystallographic plane; N_{La}, N_O denote the number of La and O atoms, respectively, in the La_2O_3(100) surface model.

μ_{La} and μ_O denote the chemical potentials of La and O atoms, respectively. For the bulk La_2O_3, the equation is as follow:

$$\mu^{bulk}_{La_2O_3} = 2\mu_{La} + 3\mu_O \quad (5)$$

where $\mu^{bulk}_{La_2O_3}$ represents the energy of the La_2O_3 solid-phase unit; $\mu^{bulk}_{La_2O_3}$ represents the energy of the bulk La_2O_3.

After combining (4), (5), the mathematical expression for $\sigma_{La_2O_3(100)}$ that exclusively depends on a single variable, μ_O can be expressed as follow:

$$\sigma_{La_2O_3(100)} = \frac{1}{2A}[E_{slab} - \frac{N_{La}}{2}\mu^{bulk}_{La_2O_3} - (N_O - \frac{3}{2}N_{La})\mu_{La}] \quad (6)$$

The surface energy calculation results for the La_2O_3(100) surface model are displayed in Table 5. When the number of the surface layers is larger than 10, the surface energy of the O-terminated model of the La_2O_3(100) surface converges to 1.769 J/m^2; Similarly, with more 13 surface layers, the surface energy of the OLa-terminated La_2O_3(100) surface model converges to 2.823 J/m^2.

The surface energy of γ-TiAl (100) can be calculated by the Botteger formula [39]:

$$\sigma = \frac{1}{2A}\left(E_{slab}^{N} - N\,\Delta\,E\right) \tag{7}$$

$$\Delta E = \frac{1}{2}\left(E_{slab}^{N} - E_{slab}^{N-2}\right) \tag{8}$$

where σ denotes the surface energy of the model; A represents the surface area of the model; and E_{slab}^{N} and E_{slab}^{N-2} respectively indicate the total energy of surface models containing N layers and N-2 layers of atoms.

The calculation results of the surface energy for γ-TiAl(100) are listed in Table 6, which indicates that when the number of surface layers is larger than 7, the energy converges to 3.080 J/m² for Al-terminated interfaces and 1.168 J/m² for Ti-terminated interfaces.

3.2. Interface model constructing

Based on criteria from mismatch and surface convergence tests, four interface models were constructed with different terminations, as illustrated in Fig. 8. These interfaces are sequentially named as O-Al, O-Ti, OLa-Al, and OLa-Ti. During the interface modeling constructing process, the optimal interface spacing was determined by assessing the relationship between spacing and structural energy. Subsequently, the relaxation and energy calculations were conducted for two types of the interface models with spacings ranging from 1.0 to 5.0 Å (increments of 0.1 Å). The relationship between energy variations among the four interfaces and interface spacing are shown in Fig. 9. All four interface structures initially exhibit decreasing energy followed by an increase. For the O-Al and O-Ti interfaces, the system energy is minimized at a spacing of 1.7 Å. For the OLa-Al interface, the minimum energy occurs at 3.1 Å spacing, whereas for the OLa-Ti interface, it is at 2.2 Å.

The interface stability strength can be analyzed in terms of interfacial adhesion energy W_{ad}. The interfacial adhesion energy is defined as the reversible work required to separate an interface into two free surfaces, and its magnitude signifies the strength of the interface structure. The calculational formula for W_{ad} is as follow [40], [41], [42]:

$$W_{\mathrm{ad}} = \frac{1}{A}\left(E_{Surface(s)} + E_{Surface(n)} - E_{Interface}\right) \tag{9}$$

where, $E_{Surface(s)}$ is the total energy of the isolated surface model of the substrate phase; $E_{Surface(n)}$ is the total energy of the isolated surface model of the nucleating phase; $E_{Interface}$ refers to the total energy of the interface model; and A represents the area of the interface.

Another criterion for interface stability is the interfacial energy *γ*. The *γ* represents the resistance encountered when forming heterogeneous interface structures and plays a crucial role in nucleation processes. The magnitude of *γ* corresponds to the difficulty of heterogeneous nucleation at the interface. Generally, a smaller *γ* indicates a more stable interface structure. The calculational formula for *γ* is as follow [43]:

$$\gamma = \sigma_{La_2O_3} + \sigma_{TiAl} - W_{ad} \quad (10)$$

where W_{ad} is the adhesion energy of the La_2O_3/γ-TiAl interface; $\sigma_{La_2O_3}$ and $\sigma_{\gamma-TiAl}$ are the surface energies of La_2O_3 and γ-TiAl, respectively.

The ideal interfacial adhesion energies W_{ad} and interfacial energies γ for the four interface models are listed in Table 7. It can be found that the W_{ad} are as follows: $W_{adO\text{-}Al} > W_{adO\text{-}Ti} > W_{adOLa\text{-}Al} > W_{adOLa\text{-}Ti}$; and the γ are ordered as follows: $\gamma_{O\text{-}Ti} < \gamma_{O\text{-}Al} < \gamma_{OLa\text{-}Ti} < \gamma_{OLa\text{-}Al}$. Among these, the W_{ad} of the O-Al interface is the highest at 5.062 J/m^2, which indicates that the adhesion strength of the O-Al interface surpasses those of the other three interfaces. It suggests that the O-Al interface structure exhibits the most robust interfacial adhesion capability. In comparison to the OLa-Al and OLa-Ti interfaces, the interface energies both the O-Al and O-Ti interface structures are negative, which indicates the minimal resistance during the formation of the interface structure, and allows for spontaneous formation.

Based on the calculations of the interface adhesion and formation energies, it is determined that La_2O_3 can effectively serve as a heterogeneous nucleation substrate for γ-TiAl. Furthermore, the heterogeneous nucleation interfaces tend to predominantly form O-Ti type interfaces. When external conditions enable the formation of all four interface structures, the adhesion strength of the O-Al type interface structure will surpass that of the O-Ti type interface structure. The O-Al type interface structure exhibits greater resistance to being separated into two free surfaces.

3.3.1. Electron Localization Function of La_2O_3(100) and γ-TiAl(100)

The Electron Localization Function (ELF) can be employed to qualitatively characterize the localized distribution of electrons and aid in verifying bond types. The calculational formula for ELF is as follow [44]:

$$ELF = 1/\left[1 + \left(\frac{D_{(r)}}{Dh_{(r)}}\right)^2\right] \quad (9)$$

where D(r) is the real electron gas density; Dh(r) is the uniform electron gas density. ELF values range from 0 to 1. When ELF = 1, electrons are fully localized; when ELF = 1/2, electrons are in a uniform electron gas state; and when ELF = 0, electrons are completely delocalized (or absent in this context).

The ELF of the La_2O_3(100)/γ-TiAl(100) interfaces are shown in Fig. 10. It can be observed that the ELF values around the O atom near the interfaces are approximately 0.85, which indicates localized electron states around the O atom. Specifically, Fig. 10**(a)** is the ELF of the O-Al type interface, where the ELF values around the Al atom near the interface are very low, which suggests minimal electron presence around Al atom and indicates the formation of ionic bonds between O and Al atom. Fig. 10**(b)** is the ELF map of the O-Ti type interface, which reveals ELF values around Ti atom near the interface of about 0.3, and around O atom and Ti atom about 0.2, and it indicates primarily ionic bonding between them. Fig. 10**(c)** is the ELF map of the OLa-Al type interface, which shows ELF values around O and Al atoms near the interface ranging from 0.2 to 0.4, and suggests the presence of the ionic bonding between them. Fig. 10**(d)** is the ELF map of the OLa-Ti type interface, which show similar results to Fig. 10**(b)**, and it indicates primarily ionic bonding between O and Ti atoms.

3.3.2. Density of states of La_2O_3(100) and γ-TiAl(100)

Based on the analysis of the interface electronic structure, the constructed interface structure displays significant localization features in the 1–3 at. layers near the interface. Therefore, the partial density of states (PDOS) of the atoms within the 1–3 layers near the La_2O_3/γ-TiAl interface was examined, and the computational results are shown in Fig. 11, with the position of the Fermi level marked by the black dashed line. It is evident that the density of states at the Fermi level near the interface is non-zero, which indicates that the chemical bonds formed at the interface exhibit some metallic characteristics.

Fig. 11**(a)** is the interface density of states (DOS) for the O-Al type interface. It is evident that the peak in the density of states at the Fermi level predominantly arises from Al atom p orbitals, supplemented by contributions from O atom s and p orbitals. Within the La_2O_3 layer beneath the interface, the density of states for O atom orbitals in the immediate interface layer is lower than those in the subsequent layer. The resonance between Al atom p orbitals near the interface and O atom p orbitals below the interface occurs in the energy range of −7.5 eV to −5 eV. Additionally, the resonance between Ti-d orbitals in the upper sublayer and O-s orbitals below the interface is observed in the range of −22.5 eV to −17.5 eV, which indicates the formation of the covalent or ionic bonds near the interface. These results substantiate the generation of Al-O bonds.

Fig. 11**(b)** is the interface DOS for the O-Ti type interface. It is observed that within the La_2O_3 layer, the density of states for O atom orbitals in the immediate interface layer is higher than those in the subsequent layer. Additionally, the resonance occurs between Ti-d orbitals in the upper sublayer and O-s orbitals below the interface in the energy range of −21 eV to −18 eV, with a more significant contribution from the peak in O-s orbital density. In the range of −7.5 eV to −2.5 eV, the resonance is observed between Al-s orbitals in the upper sublayer and La-d orbitals below the interface, which indicates the formation of the covalent or ionic bonds near the interface. These observations,

combined with electron localization function analysis, confirm the formation of Ti-O bonds.

Fig. 11**(c)** is the interface DOS for the OLa-Al type interface. It is evident that the peak in the density of states near the interface primarily originates from contributions of Al-p and O-p orbitals. Moreover, in the energy range from −5 eV to the Fermi level, the peak shape of Al-p orbitals above the interface is consistent with the upper sublayer Ti-s orbitals, which shows comparable peak values.

Fig. 11**(d)** is the interface DOS for the OLa-Ti type interface. It can be seen that the peak in the density of states at the Fermi level primarily arises from contributions of Ti-d orbitals. Within the energy range of −7.5 eV to −2.5 eV, the resonance between O-p orbitals near the interface and Ti orbitals above the interface is observed, which indicates the formation of covalent or ionic bonds near the interface. This confirms the generation of Ti-O bonds.

4. Conclusions

(1)γ-TiAl exhibits weak anisotropy, whereas La_2O_3 demonstrates a higher degree of anisotropy. The anisotropy of the volume modulus is the minimum for γ-TiAl, which is 1.09, while for La_2O_3, the Young's modulus anisotropy is the highest, which is 3.55.

(2)The mismatch between the La_2O_3(100) and γ-TiAl(100) crystal faces is the minimum, which is 4.36 %. It indicates that La_2O_3 effectively serves as a heterogeneous nucleation substrate for γ-TiAl.

(3) The interfacial binding energies for the four interface models rank as follows: $W_{adO\text{-}Al}>W_{adO\text{-}Ti}>W_{adOLa\text{-}Al}>W_{adOLa\text{-}Ti}$, and the interfacial energies are ordered as: $\gamma_{O\text{-}Ti}<\gamma_{O\text{-}Al}<\gamma_{OLa\text{-}Ti}<\gamma_{OLa\text{-}Al}$. The highest interfacial binding energy, W_{ad}, is observed for the O-Al interface structure, which is 5.062 J/m^2, while the lowest interfacial energy, γ belongs to the O-Ti interface structure, which is −3.300 J/m^2. The heterogeneous nucleation interfaces predominantly favor the O-Ti type, while the O-Al type proves the most stable.

(4)The ionic bonding primarily characterizes the bonding in the four interface structures between O-Al and O-Ti.

Acknowledgements

The authors would like to express their gratitude for projects supported by the National Natural Science Foundation of China (No. 52371077) and the Innovative Funding Project for Doctoral Postgraduates of Hebei Province, China (No. CXZZBS2024055).

References

[1] X.H. Wu Review of alloy and process development of TiAl alloys Intermetallics, 14 (2006), pp. 1114-1122

[2] M. Yamaguchi, H. Inui, K. Ito High-temperature structural intermetallics Acta Mater., 48 (2000), pp. 307-322

[3] H. Clemens, S. Mayer Design, Processing, microstructure, properties, and applications of advanced intermetallic TiAl Alloys Adv. Eng. Mater., 15 (2013), pp. 191-215

[4] X.W. Liu, Z.L. Zhang, R. Sun, F.C. Liu, Z.T. Fan, H.Z. Niu Microstructure and mechanical properties of beta TiAl alloys elaborated by spark plasma sintering Intermetallics, 55 (2014), pp. 177-183

[5]C. Kenel, A. Lis, K. Dawson, M. Stiefel, C. Pecnik, J. Barras, A. Colella, C. Hauser, G.J. Tatlock, C. Leinenbach, K. Wegener Mechanical performance and oxidation resistance

of an ODS γ-TiAl alloy processed by spark plasma sintering and laser additive manufacturing Intermetallics, 91 (2017), pp. 169-180

[6]T. Novoselova, S. Malinov, W. Sha, A. Zhecheva High-temperature synchrotron X-ray diffraction study of phases in a gamma TiAl alloy Mat. Sci. Eng. A-Struct., 371 (2004), pp. 103-112

[7]D. Hu, X. Wu, M.H. Loretto Advances in optimisation of mechanical properties in cast TiAl alloys Intermetallics, 13 (2005), pp. 914-919

[8] B.P. Bewlay, S. Nag, A. Suzuli, M.J. Weimer TiAl alloys in commercial aircraft engines Mater. High. Temp., 33 (2016), pp. 549-559

[9] J.P. Lin, L.L. Zhao, G.Y. Li, L.Q. Zhang, X.P. Song, F. Ye, G.L. Chen Effect of Nb on oxidation behavior of high Nb containing TiAl alloys Intermetallics, 19 (2011), pp. 131-136

[10] J.Y. Kim, E.S. Park, T. Lee, S. Ryu, S.E. Kim, S.W. Kim Origin of enhanced room temperature ductility in TiAl alloys: Reducing activation difference of eformation mechanism of γ phase J. Alloy. Compd., 899 (2022), Article 163307

[11] H.Y. Yasuda, T. Nakano, J. Nakazawa, Y. Umakoshi Effect of V and Nb addition on the fatigue behaviour of TiAl polysynthetically twinned crystals Isij. Int, 37 (1997), pp. 1210-1217

[12] S.L. Shu, F. Qiu, C.Z. Tong, X.N. Shan, Q.C. Jiang Effects of Fe, Co and Ni elements on the ductility of TiAl alloy J. Alloy. Compd., 617 (2014), pp. 302-305

[13] Y. Pan, X. Lu, T.L. Hui, C.C. Liu, W. Xu, C. Zhang, J.Z. Sun, X.H. Qu, J.Z. Zhang

High-temperature oxidation behaviour of TiAl alloys with Co addition J. Mater. Sci., 56 (2021), pp. 815-827

[14] S.L. Xiao, L.J. Xu, Y.Y. Chen, H.B. Yu Microstructure and mechanical properties of TiAl-based alloy prepared by double mechanical milling and spark plasma sintering T. Nonferr Met. Soc., 22 (2012), pp. 1086-1091

[15] T.T. Cheng The mechanism of grain refinement in TiAl alloys by boron addition—an alternative hypothesis Intermetallics, 8 (2000), pp. 29-37

[16] J.J. Dai, J.Y. Zhu, C.Z. Chen, F. Weng High temperature oxidation behavior and research status of modifications on improving high temperature oxidation resistance of titanium alloys and titanium aluminides: a review J. Alloy. Compd., 685 (2016), pp. 784-798

[17] K. Hamano, S. Ohta, Y. Ozaki Effects of rare earth oxides on sintering of alumina J. Ceram. Soc. Jpn., 87 (1979), pp. 632-641

[18]A.M. Thompson, K.K. Soni, H.M. Chan, M.P. Harmer, D.B. Williams, J.M. Chabala, R. Levi-Setti Dopant distributions in rare-earth-doped alumina J. Am. Ceram. Soc., 80 (1997), pp. 373-376

[19] A.E. Medvedev, M.Y. Murashkin, N.A. Enikeev, R.Z. Valiev, P.D. Hodgson, R. Lapok Enhancement of mechanical and electrical properties of Al-RE alloys by optimizing rare-earth concentration and thermo-mechanical treatment J. Alloy. Compd., 745 (2018), pp. 696-704

[20] K.L. Wang, Q.B. Zhang, M.L. Sun, Y.M. Zhu Effect of laser surface cladding of ceria on the wear and corrosion of nickel-based alloys Surf. Coat. Tech., 96 (1997), pp. 267-271

[21] T.F. Xiang, M.X. Zhang, C. Li, C.D. Dong, L. Yang, W.M. Chan CeO_2 modified SiO_2 acted as additive in electrodeposition of Zn-Ni alloy coating with enhanced corrosion resistance J. Alloy. Compd., 736 (2018), pp. 62-70

[22] G.M. Zhao, K.L. Wang Effect of La_2O_3 on corrosion resistance of laser clad ferrite-based alloy coatings Corros. Sci., 48 (2006), pp. 273-284

[23] Z.J. Shi, Y.G. Meng Effects of indentation depth and grain size on scratching behavior of nanograin FCC Fe polycrystalline substrate Tribol. Int., 193 (2024), Article 109464

[24] L.X. Rao, G. Tang, J.W. Hong Electronic and mechanical properties of ScXI (X=S, Se) monolayers and their heterostructures Phys. Rev. Mater., 7 (2023), Article 014010

[25] X. Pei, M.N. Yuan, F.Z. Han, Z.Y. Wei, J. Ma, H.L. Wang, X.Q. Shen, X.S. Zhou Investigation on tensile properties and failure mechanism of Al(111)/Al_3Ti(112) interface using the first-principles method Vacuum, 196 (2022), Article 110784

[26] J.H. Dai, Y. Song, R. Yang Influence of alloying elements on stability and adhesion ability of TiAl/TiO_2 interface by first-principles calculations Intermetallics, 85 (2017), pp. 80-89

[27] B.Y. Tong, L.J. Sham Application of a self-consistent scheme including exchange and correlation effects to atoms Phys. Rev. B., 144 (1966), p. 1

[28] G. Kresse, J. Furthmüller Efficient iterative schemes for ab initio total-energy calculations using a plane-wave basis set Phys. Rev. B., 54 (1996), pp. 11169-11186

[29] J.P. Perdew, K. Burke, M. Ernzerhof Generalized gradient approximation made simple Phys. Rev. Lett., 77 (1996), p. 3865

[30] P.E. Blöchl Projector augmented-wave method Phys. Rev. B., 50 (1994), p. 17953

[31] H.J. Monkhorst, J.D. Pack Special points for Brillouin-zone integrations Phys. Rev. B., 13 (1976), p. 5188

[32] J. Gouteron, D. Michel, A.M. Lejus, J. Zarembowitch Raman spectra of lanthanide sesquioxide single crystals: correlation between A and B-type structures J. Solid. State Chem., 38 (1981), pp. 288-296

[33] C. Wei, J.L. Fan, H.R. Gong Structural, thermodynamic, and mechanical properties of bulk La and A-La_2O_3 J. Alloy. Compd., 618 (2015), pp. 615-622

[34] R.R. Zope, Y. Mishin Interatomic potentials for atomistic simulations of the Ti-Al system Phys. Rev. B, 68 (2003), Article 024102

[35] J.H. Tan, K.J. Zhu, J.H. Peng First-principles simulation on structure property of Ti-Al intermetallic compounds J. Comput. Phys., 34 (2017), p. 365

[36] R. Hill The elastic behaviour of a crystalline aggregate Proc. Phys. Soc. A., 65 (1952), p. 349

[37] M.Q. Liao, Y. Liu, L.J. Min, Z.H. Lai, T.Y. Han, D.N. Yang, J.C. Zhu Alloying effect on phase stability, elastic and thermodynamic properties of Nb-Ti-V-Zr high entropy alloy Intermetallics, 101 (2018), pp. 152-164

[38] B.L. Bramfitt The effect of carbide and nitride additions on the heterogeneous nucleation behavior of liquid iron Metal. Trans., 1 (1970), pp. 1987-1995

[39] J.C. Boettger Nonconvergence of surface energies obtained from thin-film calculations Phys. Rev. B., 49 (1994), p. 16798

[40] Y.J. Xian, R.Z. Qiu, X. Wang, P.C. Zhang Interfacial properties and electron structure of Al/B4C interface: a first-principles study J. Nucl. Mater., 478 (2016), pp. 227-235

[41] S.Q. Wang, H.Q. Ye Theoretical studies of solid–solid interfaces Curr. Opin. Solid St M., 10 (2006), pp. 26-32

[42] W. Choe, G.J. Miller, E.M. Levin Crystal structure and magnetism of Gd_2MgGe_2 J. Alloy. Compd., 329 (2001), pp. 121-130

[43] J.R. Smith, W. Zhang Stoichiometric interfaces of Al and Ag with Al_2O_3 Acta Mater., 48 (2000), pp. 4395-4403

[44] A.D. Becke, K.E. Edgecombe A simple measure of electron localization in atomic and molecular systems J. Chem. Phys., 92 (1990), pp. 5397-5403

Table 1. Parameters of bulk, surface and interface for density functional calculation.

System	Encut (eV)	Kpoints
Bulk La_2O_3	500	7×7×7
Bulk γ-TiAl	500	5×5×5
La_2O_3 Surface	500	7×7×1
γ-TiAl Surface	500	5×5×1
La_2O_3/γ-TiAl Interface	500	7×7×1

Table 2. Anisotropy of elastic parameters of γ-TiAl.

	Bulk modulus GPa		Young's modulus GPa		Shear modulus GPa		Poisson's ratio	
γ-TiAl	B_{min}	B_{max}	E_{min}	E_{max}	G_{min}	G_{max}	ν_{min}	ν_{max}
	114.15	124.40	121.15	188.50	53.96	76.00	0.24	0.33
anisotropy	1.09		1.56		1.41		1.375	

Table 3. Anisotropy of elastic parameters of La_2O_3.

	Bulk modulus GPa		**Young's modulus GPa**		**Shear modulus GPa**		**Poisson's ratio**	
La_2O_3	B_{min}	B_{max}	E_{min}	E_{max}	G_{min}	G_{max}	ν_{min}	ν_{max}
	66.74	210.91	61.88	219.77	25.40	59.77	0.24	0.44
anisotropy	3.16		3.55		2.35		1.83	

Table 4. Lattice mismatch of La_2O_3 and γ-TiAl.

Matching face	**La_2O_3(100) / γ-TiAl(100)**			**La_2O_3(110) /γ-TiAl(100)**		
La_2O_3[uvw]	[001]	$[0\bar{2}0]$	$[0\bar{2}1]$	[001]	$[1\bar{1}0]$	$[1\bar{1}1]$
γ-TiAl[uvw]	[020]	[002]	[022]	[020]	[002]	[022]
θ **(°)**	0	0	3.298	0	0	7.359
$d_{La_2O_3}$ **(Å)**	6.204	7.896	10.021	6.204	6.815	9.216
$d_{\gamma-TiAl}$ **(Å)**	5.683	8.131	9.920	5.683	8.131	9.920
δ (%)	4.36			11.07		

Table 5. Surface energy of La_2O_3 (100) surface.

Layer	4	7	10	13	16
O-Terminated	1.669	1.765	1.769	1.769	1.769
OLa-Terminated	2.697	2.743	2.755	2.823	2.784

Table 6. Surface energy of γ-TiAl (100) surface.

Layer	5	7	9	11	13
Al-Terminated	2.885	3.080	3.007	2.963	2.945
Ti-Terminated	1.069	1.168	1.143	1.182	1.110

Table 7. The W_{ad} and γ values for the $La_2O_3(100)$/ γ-TiAl(100) interface model.

Interface model	**O-Al**	**O-Ti**	**OLa-Al**	**OLa-Ti**
W_{ad}**(J/m^2)**	5.062	3.237	2.309	3.109
γ(J/m^2)	−0.213	−3.300	3.594	0.882

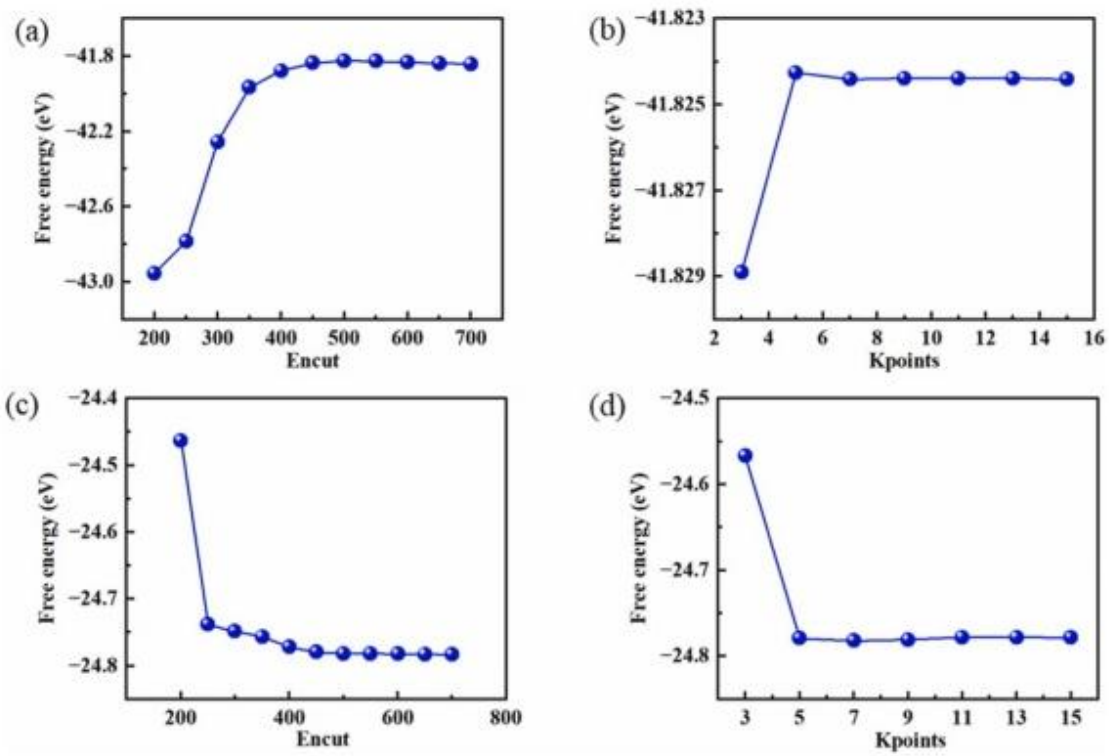

Fig. 1. Encut and Kpoints versus system energy variation.(a) La_2O_3-Encut; (b) La_2O_3-Kpoints; (c) γ-TiAl-Encut; (d) γ-TiAl-Kpoints.

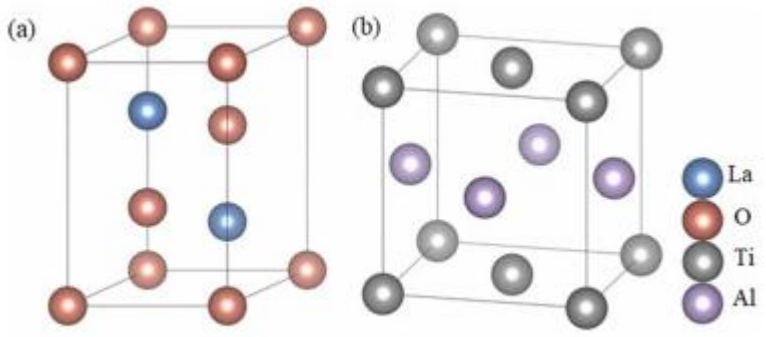

Fig. 2. Ideal crystal structure.(a)La_2O_3; (b) γ-TiAl.

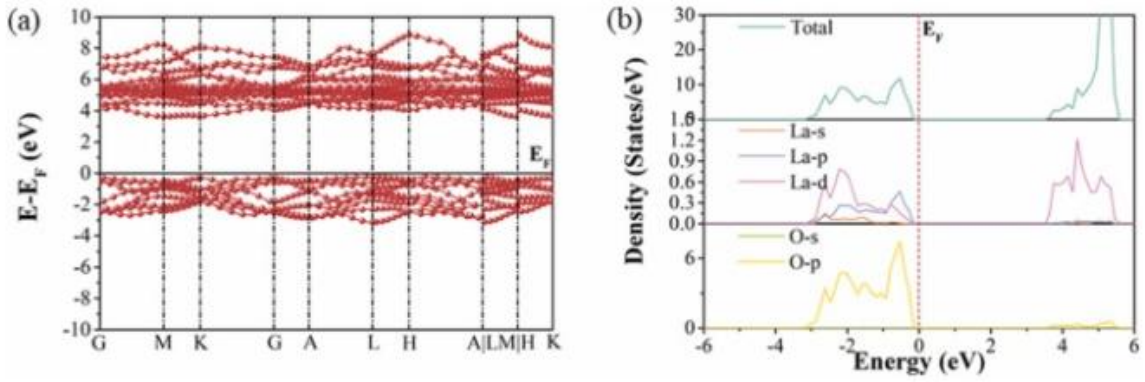

Fig. 3. Band structure and density of states of La_2O_3 (a) Band structure; (b) Density of states.

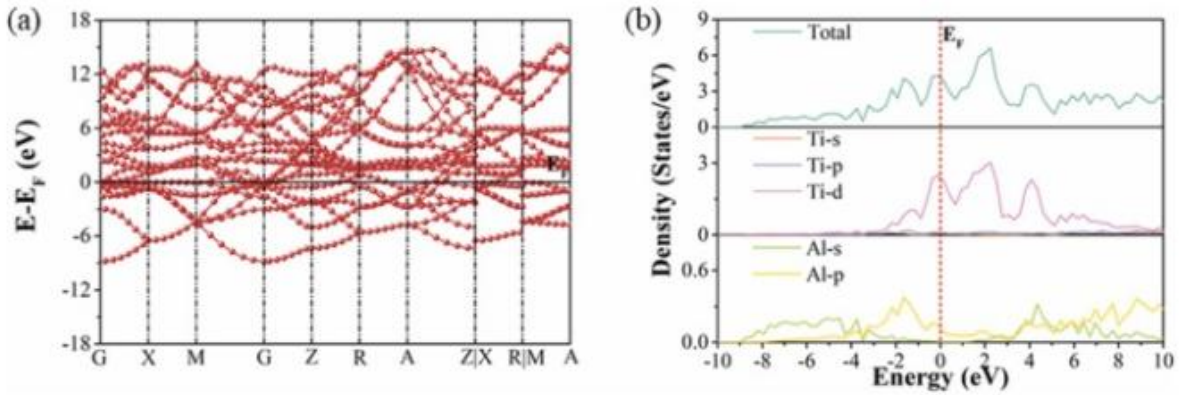

Fig. 4. Band structure and density of states of γ-TiAl (a) Band structure; (b) Density of states.

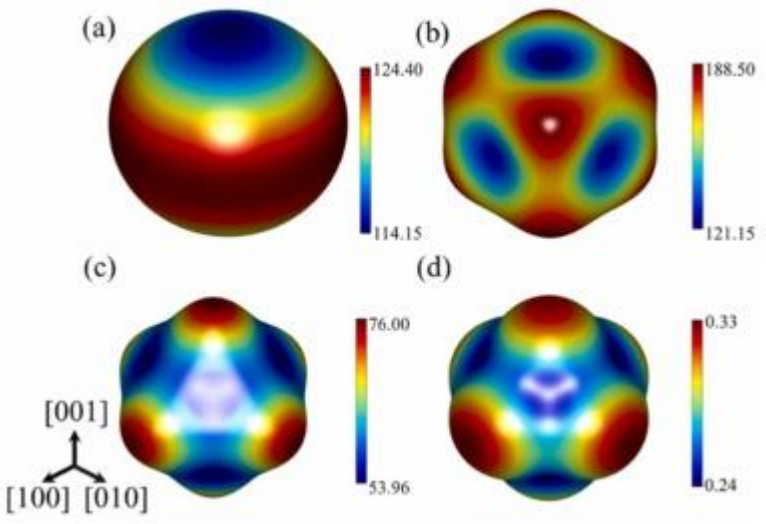

Fig. 5. 3D plots of the anisotropy of γ-TiAl(a) Bulk modulus; (b) Young's modulus; © Shear modulus; (d) Poisson's ratio.

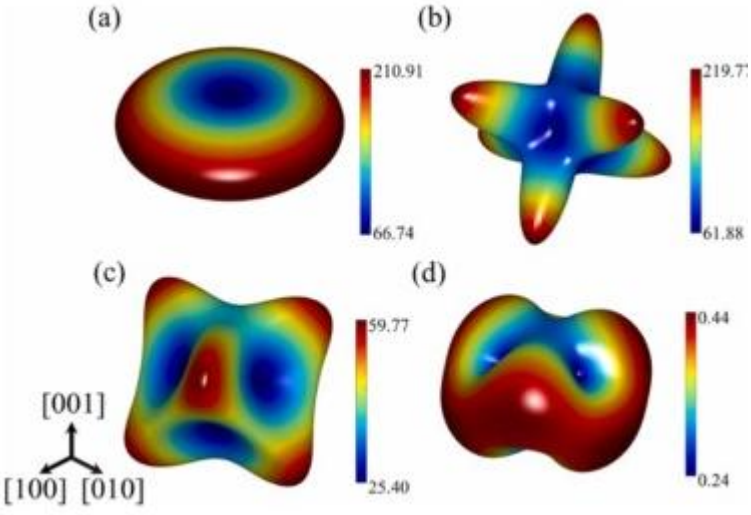

Fig. 6. 3D plots of the anisotropy of La_2O_3(a)Bulk modulus; (b) Young's modulus; © Shear modulus; (d) Poisson's ratio.

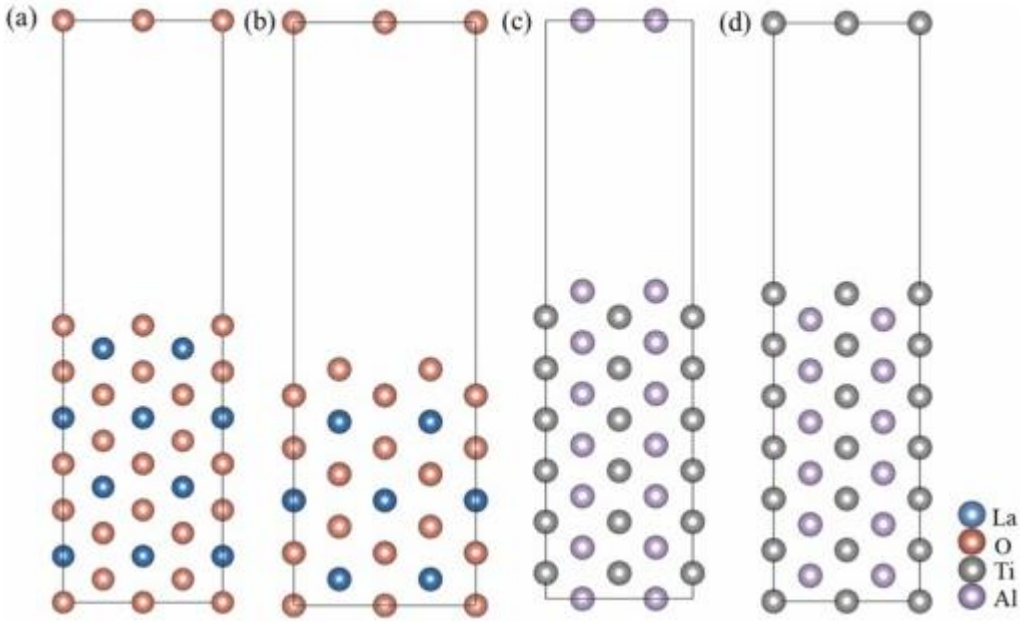

Fig. 7. Surface models of La_2O_3 and γ-TiAl (a) O-Terminated; (b) OLa- Terminated; (c) Al-Terminated; (d) Ti-Terminated.

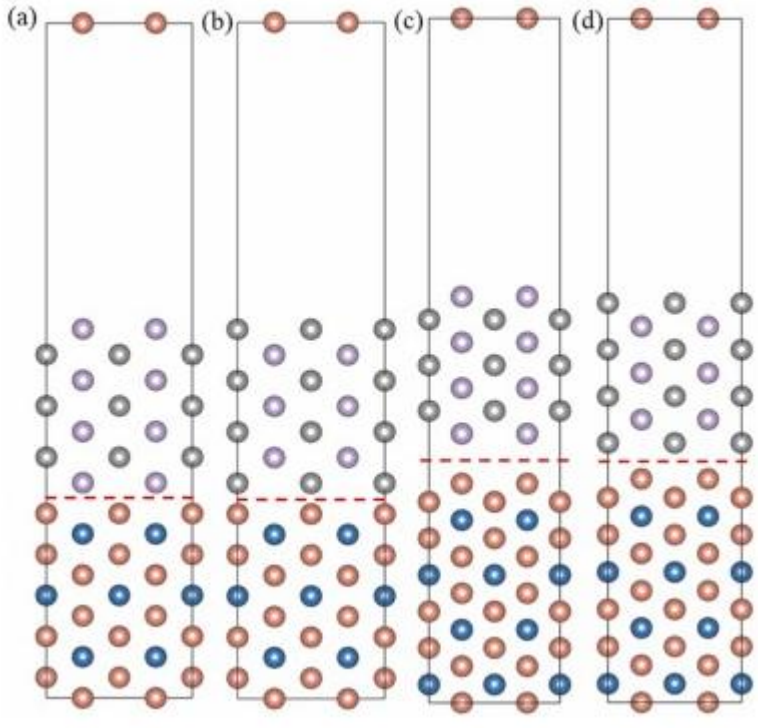

Fig. 8. Schematic diagram of four interface models(a)O-Al; (b) O-Ti; (c) OLa-Al; (d) OLa-Ti.

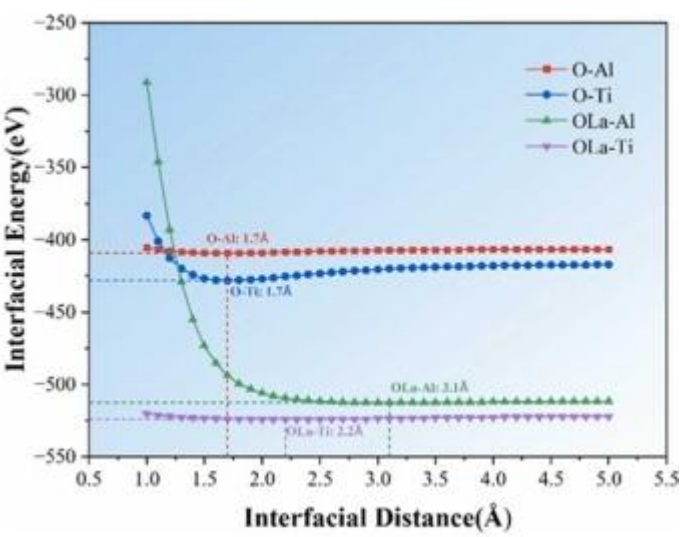

Fig. 9. Relationship between interface energy and interface spacing.

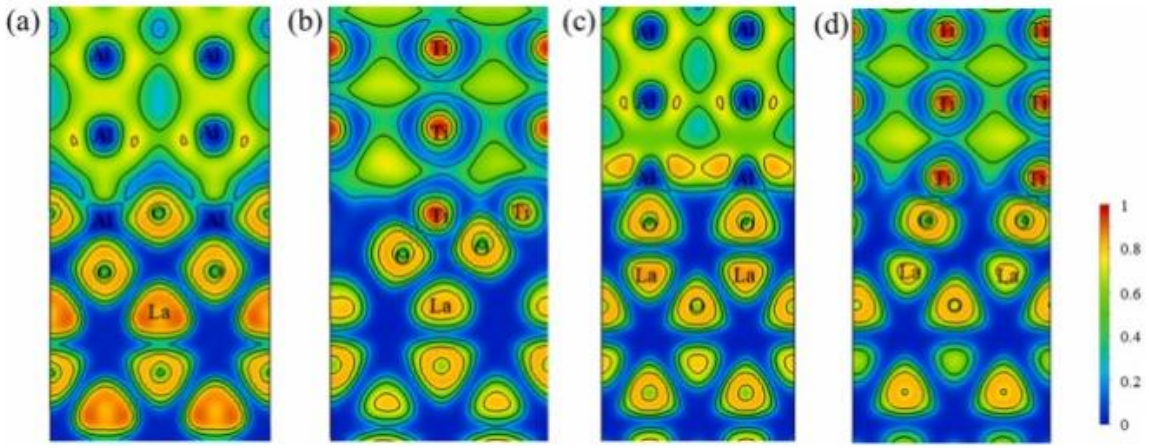

Fig. 10. ELF of the four interfaces (a) O-Al (b) O-Ti (c) OLa-Al (d) OLa-Ti.

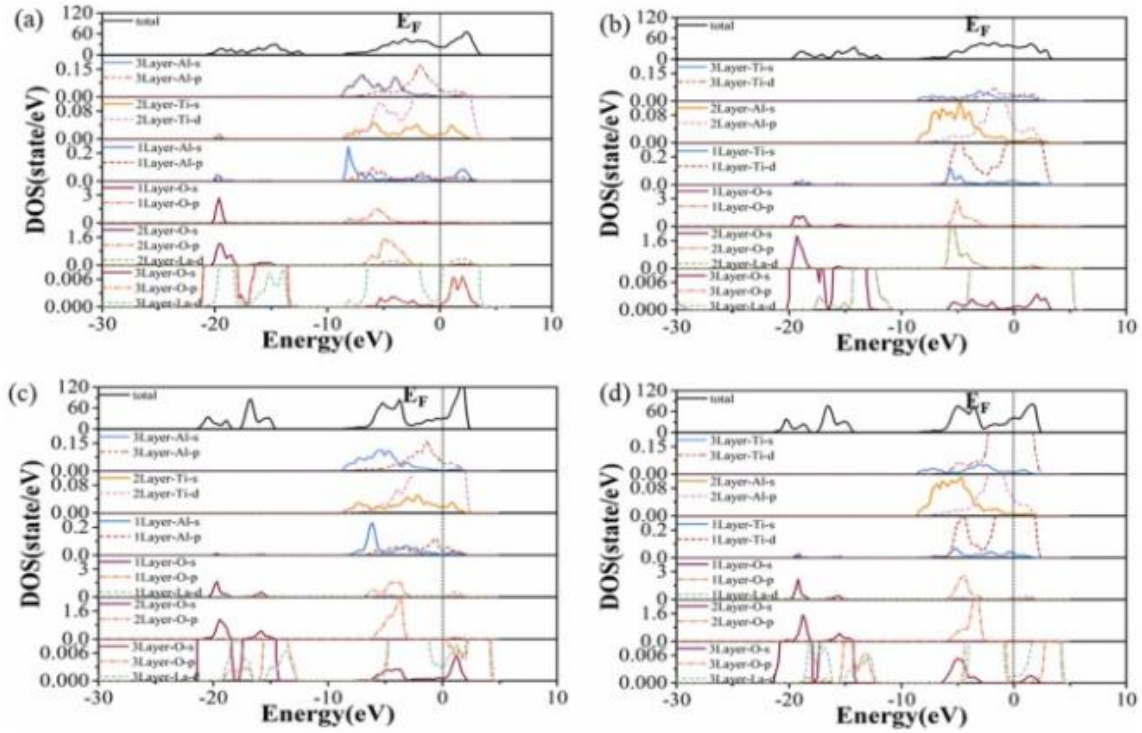

Fig. 11. The PDOS of the four interfaces (a) O-Al (b) O-Ti (c) OLa-Al (d) OLa-Ti.